Research Article | Vol. 32, No. 18 / 26 Aug 2024 / Optics Express 32448
Optics EXPRESS

Switching in microseconds: design of a 5 × 5 non-blocking free space optical switch at 1550nm with a piezo-actuator and beam-steering lens system

YANWU LIU,* TEMITOPE ODEDEYI, AND GEORGIOS ZERVAS

Optical Networks Group, Department of Electronic and Electrical Engineering, University College London, London WC1E 7JE, UK
*zczliue@ucl.ac.uk

Abstract: Modern data center networks (DCNs) require optical switches with ultra-low loss, ultra-fast reconfiguration speed, high throughput, and high extinction ratio performances. In this work, we propose the design of a 5 × 5 optical switch at 1550 nm based on a piezo-actuator serving as a translating input optical source, and a beam-steering system built of spherical lenses to complete the switching behaviour. An ultra-fast actuator switching speed is estimated as 1.55 μs latency for a single connection with a demo circuit. We further simulate the beam-steering system end-to-end in a commercial optical design software CODE V and demonstrate a theoretical 2.16 dB insertion loss for a single connection in the switch at optimum alignment.

1. Introduction

Electrical packet switching (EPS) in traditional hierarchical DCNs such as fat-tree, ring and mesh topologies suffers from legacy problems such as over-subscription, hotspots, poor flexibility, cabling complexities, limited transmission speed and high maintenance costs [1–3]. To overcome these limitations, all-optical switching technologies are introduced into modern DCNs, benefiting from their superior bandwidth in Tbps with wavelength division multiplexing (WDM), reconfigurability and the elimination of conversion process to electrical domain [4,5].

Optical switches should ideally have ultra-fast reconfiguration speed in tens of nanoseconds to be compatible with small packet sizes [6], and ultra-low insertion loss to preserve signal quality. To serve in DCNs, they should also have low crosstalk, high extinction ratio, non-blocking connectivity, large port scalability and broad operation wavelength. Current technologies include opto-mechanical switches, micro-electromechanical systems (MEMS) switches, electro-optical (EO) switches, semiconductor optical amplifier (SOA) based switches, etc [7–9]. Opto-mechanical switches redirect optical paths between trans-receiving fibres with mechanical actuation. For example, POLATIS beam-steering switch is built with rotating collimators controlled by piezo-actuators, giving a high port count of 576 × 576, a typical insertion loss of 1.5 dB and a switching latency of 75 ms [10]. MEMS actuated switches with a few microseconds of latency in light detection and ranging (LiDAR) systems have been reported in [11] at 10 × 10, and further in [12] at 128 × 128 with <5 dB loss in at least 67% out of 256 pixels tested. Silicon EO switches could operate in nanoseconds, but the unbalanced performance between Cross/Bar configuration and high sensitivity of Si-waveguides make insertion loss remains as an issue [13]. A recent development of 128 × 128 is reported in [14]. SOA switches have ultra-fast speed in sub-nanoseconds (547 ps) [6] that makes them the most promising solution to bypass the lack of optical processors in optical packet switching [15], but they also suffer from the accumulated amplified spontaneous emission (ASE) noise.

#532830 https://doi.org/10.1364/OE.532830
Journal © 2024 Received 14 Jun 2024; revised 7 Aug 2024; accepted 11 Aug 2024; published 23 Aug 2024

Optics EXPRESS

A key technology in optical switching is free space optics (FSO) that supports high data rate (Gbps) transmission with narrow line laser sources [16]. Compared with fibre optics, FSO is intrinsically robust against dispersion, nonlinearities and micro-bending. Also, FSO could deliver key characteristics such as flexible installation, low power consumption, low propagation loss (indoor), high data security, wavelength and polarisation independence that all make it very appealing for DCNs [16–19]. Many studies have been proposed to de-congest a traditionally oversubscribed DCN by augmenting steerable FSO channels onto top-of-rack (ToR) switches using Digital Micromirror Device (DMD) [20], liquid crystal/rotational mirrors [21], diffractive gratings [22], or wavelength tuning/phase shifters [3]. Whilst fast switching can be achieved as low as nanoseconds [22], these solutions also suffer from high diffraction-related loss from 6.84 dB [22] to 10.41 dB [20], or beam-spreading induced loss up to 25 dB [3] at receiving photodetectors.

In summary, existent FSO technologies such as POLATIS switches, DMD switches and MEMS switches are generally not well balanced between fast switching and low insertion loss, which limits them to specific usage, either long-life traffic or loss insensitive scenarios. In our work, we demonstrated the possibility of combining both sub-millisecond latency (as found in DMD switches) with low loss (as found in POLATIS switches) by exploiting the benefits from both piezos and lens optics. In this case, the piezo displacement and load are reduced for fast switching, whereas the beam-steering optics is used to compensate for the displacement required and to provide loss control. Therefore, our proposed switch could fill a in gap in existent technologies. It is the cumulative effect of combining these approaches that results in the performance improvements reported and therein lies the novelty of this work.

- In Section 2, we propose a 5×5 non-blocking FSO switch with an estimated 1.55 μs of switching latency, which is in orders of reduction than POLATIS switches operating in tens of milliseconds. The proposed switch combines both mechanical and optical components, including a fast piezo-actuator that laterally shifts the input fibre behind each switching port, and a novel optical beam-steering system built of spherical lenses to complete the switching path. To obtain an ultra-fast response, we minimise the mechanical switching displacement to <5 μm rather than tens of micrometers or millimeters in MEMS switches [23–25], and reduce the actuator load to a single lightweight lensed fibre rather than bulky collimators in POLATIS switch [10]. To obtain the optimal loss performance, the beam-steering lens system eliminates the usage of any diffractive optics, and is designed with aperture clipping control that minimises insertion loss.
- In Section 3, we introduce the physical layout of the switch in a non-blocking connectivity.
- In Section 4, we perform end-to-end simulations of Gaussian beam propagation for the beam-steering system in an optical design software CODE V. Whilst fabrication and experiments are beyond the scope of this work, a theoretical 2.16 dB insertion loss is expected for a single connection at optimum alignment. We then perform loss sensitivity analysis with respect to beam variations and fibre coupling. The conclusion is drawn in Section 5.

2. Design of a passive beam-steering lens system

The switch proposed in this work is an optical circuit switch, where switching is carried out by physically changing the optical propagation path. The switching mechanism is independent of wavelength, and the input signal could be either single frequency or a wavelength-division multiplexing (WDM) signal.

We first introduce a passive beam-steering lens system as the major building block inside the proposed switch to translate the piezo actuation to a steering beam. Fast beam-steering with lens

Optics EXPRESS

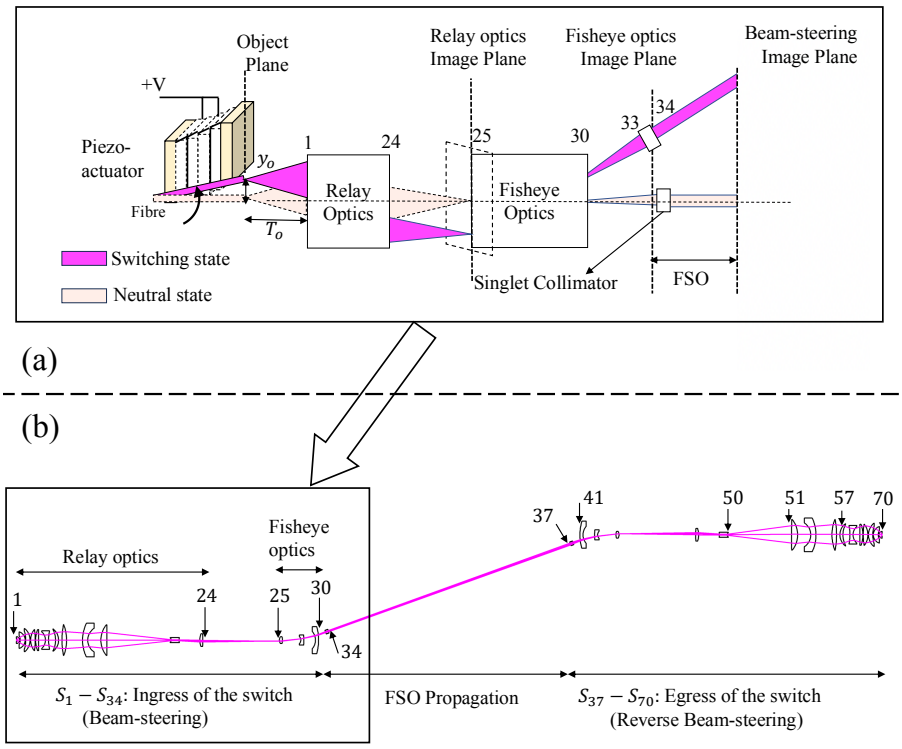

Fig. 1. (a) A beam-steering (BS) system placed at the ingress of the switch. A driving voltage $+V$ is applied to multiple deformable sheer-plates of the piezo-actuator. The accumulated deformation switches the fibre tip from the neutral state to an object height of y_o, thereby changing the physical propagation path of the optical signal regardless of wavelength. The object plane is placed at the waist of the Gaussian beam emitting from the fibre. The coloured triangular represents the changes in beam envelope as it propagates through the system. (b) An end-to-end switching path showing geometrical tracing in CODE V between two furthermost ports requiring the largest object field height $y_o = 4.77$ μm. Serial numbers represent optical surface indices where two surfaces build a singlet lens. A full labelling is given in Fig. 2.

optics has been demonstrated in LiDAR [26] and indoor optical wireless communications (OWC) [27] with channel switching time at microseconds. Figure 1(a) demonstrates the sketch diagram for the optical beam-steering (BS) system at the ingress of each port in the switch. Inspired by [28], this beam-steering optics contains 4 subsystems: a sheer-plate stack piezoelectric actuator with a lensed fibre mounted to its side surface, a relay optics, a reverse usage of fisheye optics, and an array of singlet collimators. Piezoelectric actuators are widely used in micro/nano-positioning systems with sub-nanometer resolution commercially available [29], and there are mature control strategies to compensate for their positioning errors/vibration/hysteresis and nonlinearities [29–31]. A driving voltage $+V$ is applied to the sheer plates of the piezo-actuator to switch the tip of the fibre from the neutral state to an object height of y_o. Different values of y_o would follow different propagation paths in subsequent lens system, thus completing a switching behaviour. The object plane is placed at the waist of the Gaussian beam emitting from the fibre. A relay optics with a large numerical aperture is placed at an object distance T_o in air to collect the fast diverging beam. The beam envelope is approximated as the coloured triangular. The relay optics performs a first stage of lateral displacement magnification ×60 and refocuses the

Optics EXPRESS

beam onto the Relay Image Plane (RIP). Then, this displacement is transformed into a wide beam-steering angle by a fisheye optics. Finally, a singlet micro-collimator is placed decentered and tilted from the main optical axis to provide individual collimation for each steering output to minimise beam-spreading during FSO propagation. The superposition of all singlet collimators are denoted as an array (SCA).

A complete switching path also includes a reverse usage of the beam-steering system placed at the egress of the switch, as shown in Fig. 1(b). This demonstrates an end-to-end geometrical trace in CODE V for the switching path requiring the largest object height y_o = 4.77 μm to connect between two furthermost ports in the switch, with surface index S_i as labelled. The switching path contains a total of 32 singlet spherical lenses and is symmetrically divided into the Ingress/Egress side of the switch, each containing 16 lenses. S_1-S_{34} is the beam-steering system shown in Fig. 1(a), where S_1-S_{24} is the relay optics, S_{25}-S_{30} is the fisheye optics, and S_{33}-S_{34} is the micro-collimator. S_{31}-S_{32} are dummy surfaces with infinite Y-curvature radius and only thickness for positioning purposes. $S_{35} - S_{36}$ are dummy surfaces of FSO propagation of 84 mm. S_{37}-S_{70} is the reverse usage of beam-steering system. S_{71} is the Image plane where output fibre front face should be placed at. A full labelling for each optical surface is given in Fig. 2. Dummy surfaces, object and image plane are not real lens surfaces and are not labelled.

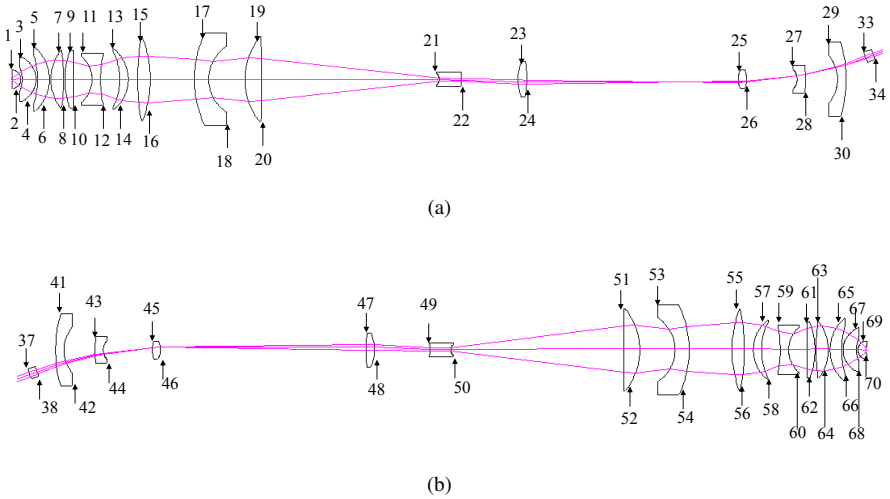

Fig. 2. Optical surface indices for (a) beam-steering system S_1-S_{34}. STOP aperture is given at S_9. (b) Reverse beam-steering system S_{37}-S_{70}. Odd number represents the front surface of a lens, whereas even number represents the rear surface. Dummy surfaces, object and image plane are not real lens surfaces and are not labelled.

2.1. Piezo-actuator performance

In this work, we aimed to push the travelling range and switching speed limit of current industrial piezo-actuators in optical switching. A demo amplifier circuit as shown in Fig. 3(a) is built to drive a customised piezo-actuator PN5FC3−18UM (Thorlabs, [32]) at its maximum respond speed. To switch between two furthermost ports as in Fig. 1(b), the piezo-actuator requires a driving voltage approximately ±125 V to achieve 50% of its maximum working range (±9 μm in ±200 V) considering 30% displacement hysteresis. This circuit is tested with the piezo-actuator connected but without fibre mounted, showing a voltage response with a mean peak-to-peak voltage of 248.43 V and a mean slew rate of 80.02 V/μs, as given in Fig. 3(b). Therefore, it could be estimated that the switching time between two furthermost ports (0 to +4.77 μm) is around

Optics EXPRESS

1.55 μs, detailed in Appendix A. In future experiments built with a physical switch, the stepwise accuracy and repeatability generated by the piezo-actuator will be measured using a digital signal input with interferometers. The cumulative impact of electrical noise, piezo hysteresis and imperfections in fibre mounting can be jointly analysed as sources of directional errors in beam propagation, which would induce more clipping loss to signal quality. This will be classified in an end-to-end communication link in future works.

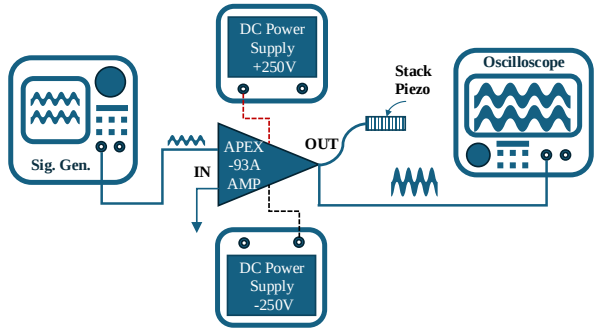

(a)

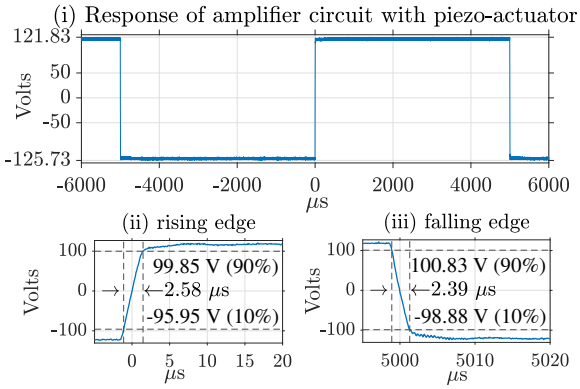

(b)

Fig. 3. (a) System diagram for the demo amplifier circuit to drive the piezo-actuator PN5FC3-18UM, detailed in Appendix A. The diagram only shows a single-axis, single-piezo set-up, whereas the actual system features multiple piezos with two-axis actuation for precise positioning. (b) Measured response from the demo setup showing mean peak-to-peak voltage of 248.43 V and a mean slew rate of 80.02 V/μs, with 10% – 90% rising and falling time labelled.

2.2. Relay optics

As the first surface of the beam-steering system, the relay optics is designed with a large numerical aperture to sufficiently capture the expanded beam radius after propagating an object distance in free space. Although not a necessary requirement, we use a Gaussian beam with a small mode field diameter (MFD) of 1.0 μm (commercially achievable with lensed fibre by LaseOptics Corporation [33]) as the input object, for better loss control than using larger beam sizes. This gives the pupil definition in CODE V as the object numerical aperture,

$$\mathrm{NA_o} = n \sin\theta = n \sin\left(\frac{2\lambda}{n\pi \mathrm{MFD}}\right) \tag{1}$$

Optics EXPRESS

where $n = 1.0$ is the vacuum refractive index, θ is Gaussian beam divergence angle and λ is the wavelength, giving $NA_o = 0.8342$ at MFD = 1 μm.

The relay optics provides lateral amplification (×60) and corrects aberrations to prevent them from being magnified by the fisheye optics as beam spreading. The relay optics adopts the concept of microscope objectives as its front lens group, and microlithographic projection lens as its middle and rear group with alternating positive and negative grouped powers [34,35]. Strong positive powers refocus the beam, but also introduce large spherical aberrations (SA). This is compensated by iteratively interleaving negative powers, which also protects lateral amplification from being destroyed by cascaded positive powers. Finally, the relay optics satisfies the near double-telecentric condition, where chief rays are always parallel to the optical axis at both object and image plane [36] to create equivalent lateral magnification for any input object heights.

2.3. Fisheye optics

As shown in Fig. 2, in the reverse Z-direction, the fisheye optics contains two negative meniscus lenses ($S_{27} - S_{30}$) that determine the field-of-view (FOV) of beam-steering, followed by a convex lens ($S_{25} - S_{26}$) that translates telecentricity from the relay optics to an incident angle. The two meniscus lenses are designed with a geometrical method reported in [37] by reversely tracing the chief ray, providing a maximum FOV of 75°.

2.4. Singlet collimator array

The output beam from fisheye optics is divergent due to wide-angle imaging [38]. Collimation is performed individually for each beam, where a micro-collimator (optimised based on LA4026-C, Thorlabs [39]) is placed with its optical axis aligned to the slope angle of beam center. A fan-out of N steering beams requires N such collimators installed as an array.

3. Design of a symmetrical non-blocking switch

Figure 4(a) shows the block diagram of a 3×3 switch in Y-axis with solid lines denoting a non-blocking connectivity. Each port is installed with a beam-steering system shown in Fig. 1(a). At any switching event, only one Gaussian beam is inputted into each port with a variable object field height (y_o) generated by piezo-actuator as labelled in Fig. 4(a). Each value of y_o invokes a unique beam-steering angle that propagates to a corresponding output port. Since optical path is reversible, the output beam from the switch should be a negative conjugate of the input beam, i.e, $w_r^o = w_r^i$ where w_r^o, w_r^i is Gaussian beam radius at the Object or Image plane, respectively; and $y_i = -y_o$, where y_i is the field height at the Image plane where output fibre should be placed at for optimal coupling. Due to symmetry, only 3 optical paths P_{31}, P_{32}, P_{33} need to exclusively designed, where P_{ij} represents Port i connects to Port j in a single direction. Any scenarios in Port 2 could reuse P_{32} and P_{33}, whereas Port 1 is exactly same as Port 3.

The scalability can further expanded by adding orthogonal axes. In this work, we limit it to 5×5 in an X-Y configuration as shown in Fig. 4(b), since 3×3 is the maximum scalability in a single axis with optimised loss performance under this set of lens parameters. Further expansion of scalability introduces more clipping loss at the edge of fisheye lenses, which requires a re-design of lenses. Cross-axis communications, such as optical path P_{41} highlighted in Fig. 4(b) where Port 4 connects to Port 1, must be enabled to maintain non-blocking connectivity with diagonal collimators. A numerical design process for all four optical paths is detailed in Appendix B. The maximum scalability of a monolithic switch is 9×9 that can be regarded as a superposition of two 5×5 switches where one of them is rotated by 45°.

Optics EXPRESS

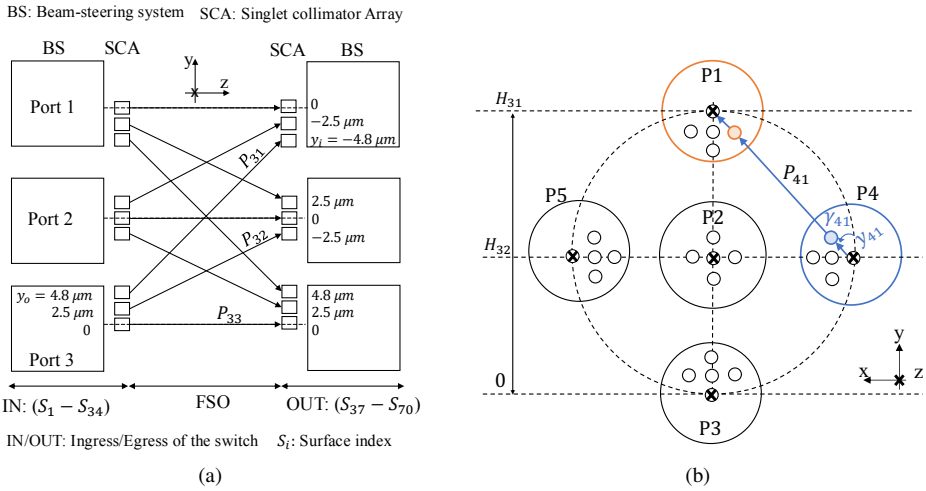

Fig. 4. (a) Non-blocking connectivity of a 3×3 switch in Y-axis. (b) Front view of cross-axis communication in a 5×5 switch. P_1 to P_5: Port 1 to Port 5. Blue: input port. Red: output port. Black cross: origin of each port in local coordinates where piezo-actuator is installed. H: global virtual image height in each switching path with $H_{31} = 2H_{32}$ (detailed in Appendix B). Large circle (dashed): Virtual plane of all vertices of fisheye optics. Medium circles (P_1 to P_5): clear aperture of each port. Small circles within each port: singlet micro-collimators.

4. End-to-end simulations of optics in CODE V

4.1. Gaussian beam propagation

We perform end-to-end simulations in CODE V separately for each possible switching path, P_{31}, P_{32}, P_{33} and P_{41}, with a small $1/e^2$ Gaussian beam radius of 0.5 μm [33] at 1550 nm as the input object. To emulate piezo-actuation, each input beam is centered at different Y-Shifts against the local origin, with P_{31} : 4.77 μm, P_{32} : 2.5 μm, P_{33} : 0 μm and P_{41} : 3.5 μm. The X-Shifts of all four beams remain 0. For simplicity, P_{41} is on a $\gamma_{41} = -45°$ tilted plane as in Fig. 4(b).

The wavefront diffraction propagation is simulated with the built-in function *Beam Synthesis Propagation (BSP)*. BSP decomposes the input field into multiple beamlets, propagating them individually through the system and summing the field at downstream. The reconstructed Gaussian beam profile at each surface is used to model clipping loss and beam divergence due to diffraction [40]. All samplings are carried out at the near field of each surface before the beam interacting with it.

Figure 5 (a-d) and Fig. 5 (e-h) demonstrate the Gaussian beam intensity sampled at the beam-steering plane (S_{31}) and Image plane (S_{71}), respectively. S_{31} is a dummy surface placed immediately after the rear surface of fisheye optics (S_{30}), proving the effectiveness of beam-steering shown as Y-Shift as labelled. S_{71} is the image plane that proves the output from the switch is also a Gaussian beam shown as the negative conjugate of the input beam, with similar mode radius but centered at opposite Y-Shifts. Their locations are shown in Fig. 6 as a sketch.

4.2. Sensitivity analysis

4.2.1. Input Gaussian beam radius variations

We increase the input Gaussian beam radius from 0.5 μm to 0.8 μm and repeat *Beam Synthesis Propagation (BSP)* to emulate the effect of the fabrication errors in lensed fibres. In BSP, beam

Optics EXPRESS

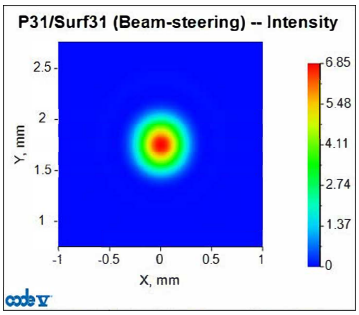

(a) P_{31}: Y= 1.75 mm

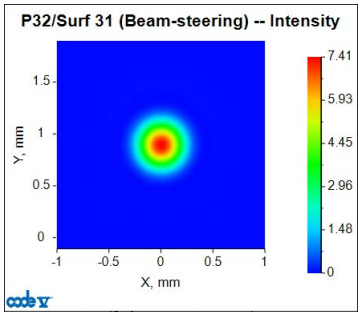

(b) P_{32}: Y= 0.89 mm

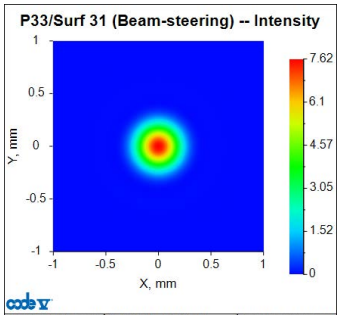

(c) P_{33}: Y= 0.0 mm

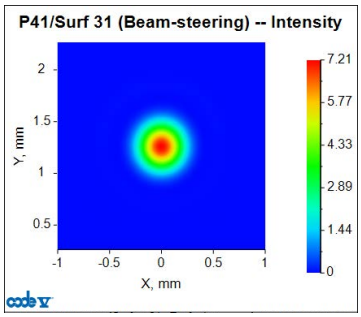

(d) P_{41}: Y= 1.26 mm

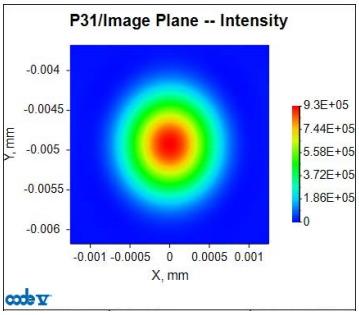

(e) P_{31}: Y= -4.93 μm

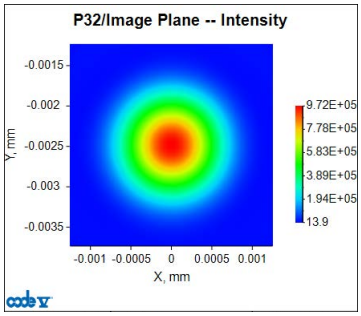

(f) P_{32}: Y= -2.49 μm

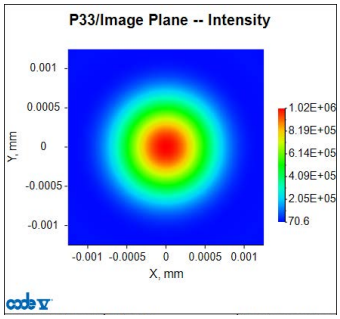

(g) P_{33}: Y= -0.0 μm

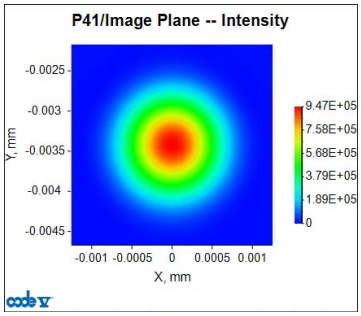

(h) P_{41}: Y= -3.42 μm

Fig. 5. Reconstructed Gaussian beam intensity in Beam Synthesis Propagation (BSP) showing: (a-d) Beam-steering from the fisheye optics (Surface 31); (e-h) Gaussian beam as the output of the switch at Image Plane (Surface 71). Each label represents the Y-Shift of beam center against local surface origin. P_{ij} represents an optical path where Port i connects to Port j in a single direction.

Optics EXPRESS

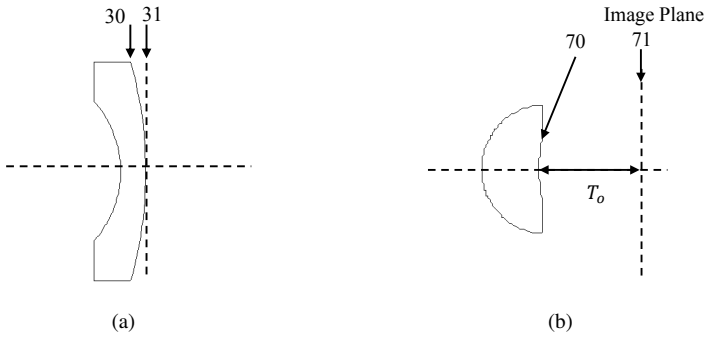

Fig. 6. (a) The location of dummy surface (S_{31}) with respect to the last optical surface of fisheye optics (S_{30}). (b) The location of image plane (S_{71}) with respect to the last optical surface of the entire switch (S_{70}). T_o is the distance to image plane same as the object distance. The sizes of lenses are not to scale.

power is computed by integrating the irradiance over the sampling grid. This value is accurate if the sampling grid covers the entire beam and the beam envelope is varying slowly at the scale of grid spacing. Figure 7 shows the near-field power sampled before beam interacting with each lens surface. Major clipping loss are identified at Surface 33, 37, 51, 57 (labelled in Fig. 2), where S_{33} and S_{37} are the front surfaces of collimators, S_{51} and S_{57} are two small clipping apertures. The reasons for power loss are categorised as:

- Small aperture clipping occurs at S_{33}, S_{34}, S_{51} and S_{57}. The power transmission ratio for a Gaussian beam radius (w_r) incident onto a circular clear aperture with radius (R_{CA}) if their centers are aligned, is given as [41],

$$T = 1 - \exp\left(-\frac{2R_{CA}^2}{w_r^2}\right) \tag{2}$$

  where clipping loss ($10\log_{10} T$) is as negligible as 0.05 dB if R_{CA}>1.5w_r [42]. The ratio of $\frac{R_{CA}}{w_r}$ in switching path P_{31} is plotted in Fig. 8, showing that S_{34} and S_{57} have the worst clipping. Nevertheless, for $\omega_r = 0.5$ μm in Fig. 8(a), all apertures are compact in size but could still maintain at least 94% transmission. When increased to 0.8 μm in Fig. 8(b), beam-spreading correspondingly increases until it matches with the clear aperture radius at the collimator (S_{34}) with 87% transmission.

- Misalignment clipping arises from imperfect positioning of collimators, showing as incident beam deviating from surface center after FSO propagation, such as S_{37}.

In summary, we define the accumulated propagation loss (L_P) up to the last optical lens surface (S_{70}) before Image plane as,

$$L_P = 10\log_{10}(P_{S_{70}}) \tag{3}$$

where $P_{S_{70}}$ is the near-field sampled power at S_{70} in Fig. 7. As shown in Fig. 9(a), an increase in beam radius from 0.5 μm to 0.8 μm would induce up to 0.38 dB more loss in L_P, which occurs in P_{31}.

4.2.2. Input Gaussian beam positioning

Piezo-actuator hysteresis and rack vibrations generate positioning errors where the center of input Gaussian beam deviates from its nominal positions. We emulate this effect in *Beam Synthesis Propagation (BSP)* by varying the input beam center with a displacement in X-axis (XDE) from

Optics EXPRESS

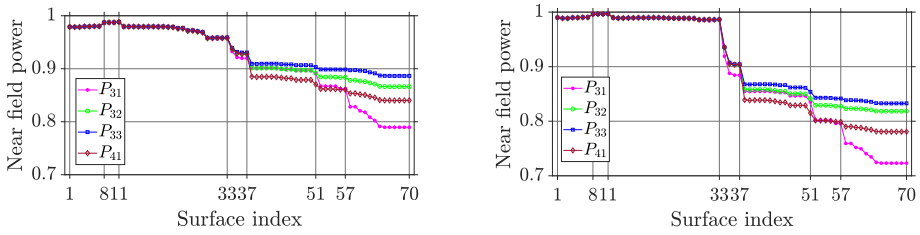

(a) Input beam radius: 0.5 μm (b) Input beam radius: 0.8 μm

Fig. 7. Near-field power sampled before beam interacting each lens surface. Object and Image plane are not included. The outliers between Surface 8 – 11 are due to limited sampling in fast changing Gaussian envelope (shown as ringings) but within <1% of prior or subsequent surfaces.

the origin. This introduces misalignments between beam center and surface center shown as the accumulated propagation loss in Eq. (3), plotted in Fig. 9(b). An XDE of 0.3 μm would induce up to 0.56 dB more loss than ideal positioning, which occurs in P_{31}.

4.2.3. Output fibre coupling efficiency

The coupling loss due to fibre positioning at the output of the switch is characterised by the build-in function *Diffraction Analysis - Fibre Coupling Efficiency (DACEF)* in CODE V. DACEF compares the complex amplitude of Gaussian beam sampled by *Beam Synthesis Propagation (BSP)* at the Image plane with a single-mode fibre [43], where we assume the fibre has a mode radius of 0.8 μm equivalent to the average beam size at Image plane, and the center of fibre front face is coincident with the beam center at Image plane. The output fibre can be sufficiently approximated as a parallel orientation, since the chief ray angle created by actuator deformation is as small as $\arctan(5\,\mu\text{m}/11.9\,\text{mm}) = 0.024°$, where 5 μm is the actuator lateral displacement and 11.9 mm is length of actuator including all sheer plates in longitudinal axis. Figure 10 demonstrates the coupling loss computed by CODE V if the output fibre center deviates in X/Y-axis from the output beam center. Since piezo-acuators intrinsically suffer from displacemental hysteresis and rack vibrations, this emphasise the usage of PID (Proportional – Integral – Derivative) control and minimum piezo-actuator step size in nm [44] to obtain a stable coupling at the switch output.

4.3. Loss analysis summary

We summarise the end-to-end insertion loss as shown in Fig. 11, including:

- Accumulated propagation loss (L_P): defined in Eq. (3) as the loss up to the last optical surface (S_{70}) before Image Plane, with labelled values listed in Fig. 9(a) (ω_r = 0.5 μm) and detailed in Section 4.2.1.
- Output fibre coupling loss: We use the theoretical optimum found in Fig. 10 at XDE = YDE = 0 as the labelled values in Fig. 11, where mode mismatch loss and fibre positioning loss are both minimised assuming a lensed fibre with mode radius equivalent to average beam size, and the fibre center is located exactly at the beam center. This does not include coupling loss due to lensed fibre tip.
- Material absorption loss: We perform the built-in function *Transmission Analysis (TRA)* in CODE V to characterise the absorption loss from glass material. In TRA, a bundle of rays is traced through the system where power transmittance is calculated for each optical element and combined at the end of the system.

Optics EXPRESS

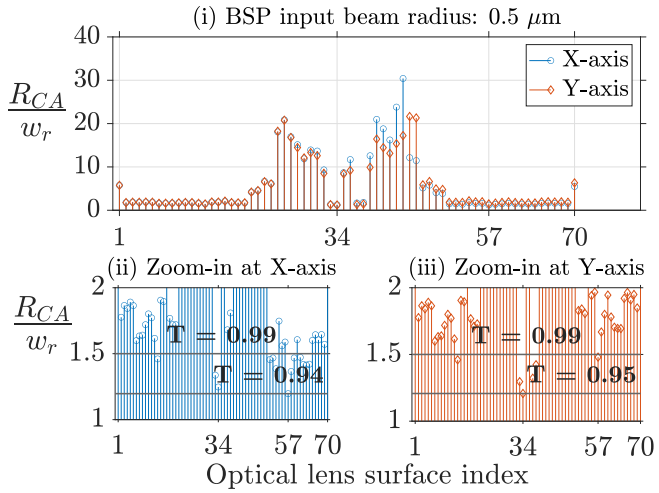

(a) Min power transmission: T = 94% (X-axis, at S_{57}) and T = 95% (Y-axis, at S_{34}).

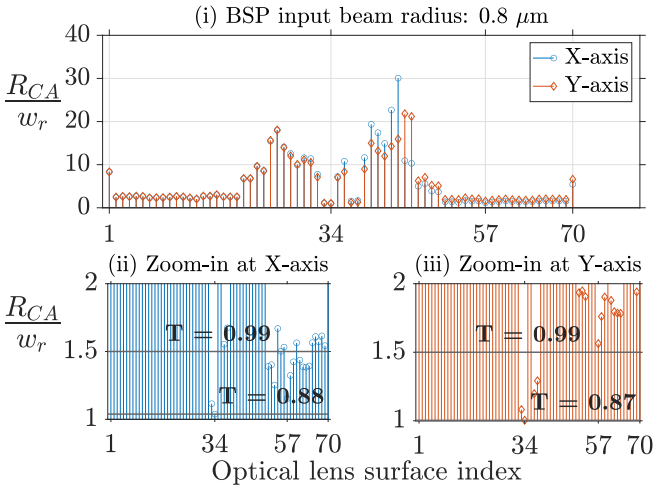

Fig. 8. Ratio of clear aperture radius to incident beam radius (by BSP best fit Gaussian) at each optical element surface for P_{31}. T is power transmittance defined in Eq. (2) and labelled in the smaller window at 99% and min values in X/Y-axis, respectively. Subfigures (i), (ii) and (iii) share the common X and Y label.

Optics EXPRESS

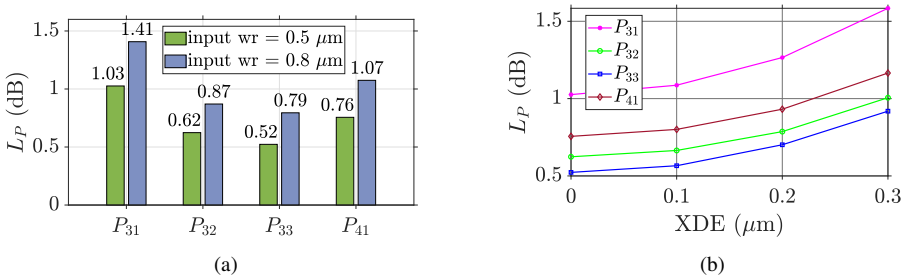

Fig. 9. Accumulated propagation loss (L_P) defined in Eq. (3), with (a) different input Gaussian beam radius w_r at object plane; (b) at w_r = 0.5 μm, if the input beam center deviates in X-axis (XDE) from the origin. XDE = 0 is the ideal positioning where values are equivalent to those in Fig. 9(a).

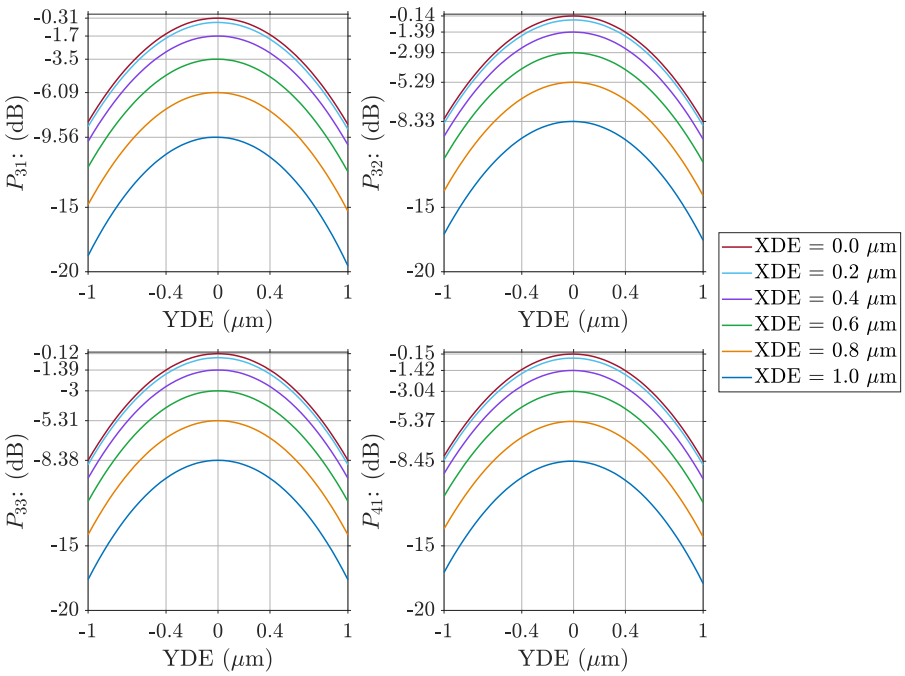

Fig. 10. Output fibre coupling loss simulated in Code V for each switching path P_{ij}, if the center of fibre front face deviates in X/Y-axis (XDE/YDE) from the beam center at the Image plane. Y-labels represent values at YDE = 0. Input Gaussian beam radius: 0.5 μm; Output fibre mode radius: 0.8 μm.

Optics EXPRESS

- Reflection loss: We assume a narrowband antireflective (V-) coating at 1550 nm with an average R<0.25% per optical surface (Thorlabs, [45]). This gives a total reflection loss of $10\log_{10}(1-R)^{64}$ across all 64 surfaces.

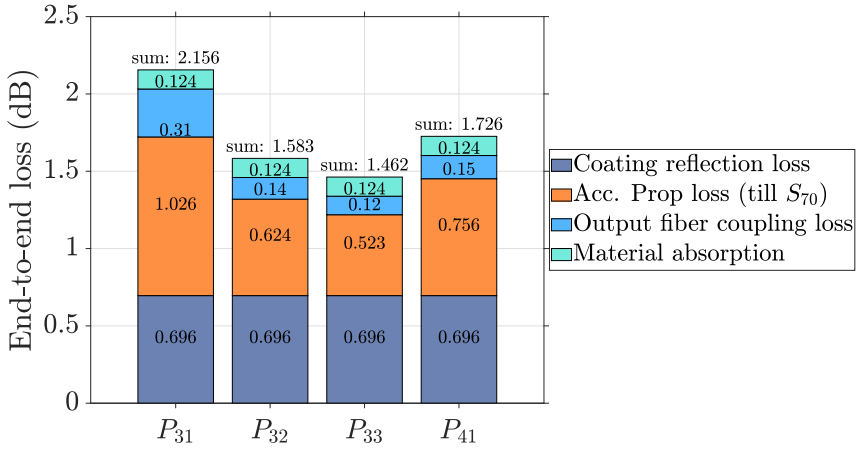

Fig. 11. End-to-end loss analysis at 1550 nm for each switching path P_{ij} with loss contributors and total sum as labelled. Object plane input Gaussian beam radius is 0.5 μm.

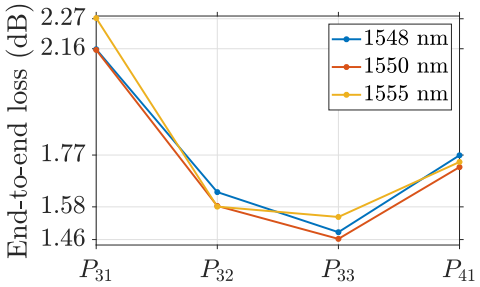

Fig. 12. Wavelength dependency on loss performance.

In summary, the switching path loss shows a positive correlation with the required piezo-actuator lateral displacement. A discussion of simulation accuracy of *Beam Synthesis Propagation* in CODE V is shown in Appendix C.

4.4. Discussions

- Wavelength dependency: Although the switching mechanism does not rely on wavelength, the loss performance is wavelength dependent due to changes in refractive indices. In this case, different wavelengths experience slightly different physical propagation path, shown as variations in loss performance in Fig. 12, where we repeated the analysis in Section 4.3 for a longer wavelength (1555 nm) and a shorter wavelength (1548 nm). This shows that the switch has a near stable loss performance within a 7 nm bandwidth, and is optimised at 1550 nm. The details of loss contributors are given in Fig. 15, Appendix D.

- Nonlinearities: Free space optics suffers less from power-induced nonlinearities than fibre optics. However, wavelength-induced aberrations may introduce image quality degradation, shape distortion and phase noise, which give more impact on phase modulated signals than

Optics EXPRESS

purely intensity modulated signals. This could be quantified with information error rate in a physical switch in future works.

- Resolution and repeatability: The resolution of a piezo-actuator is mostly limited by electrical noise, since its deformation involves changes of dipoles in response to electrical charges, free of mechanical friction [29,30]. Commercial piezo-actuators have resolutions ranging from nanometers to subnanometers [29] which are sufficient to cover the alignment requirement of 0.3 μm in Fig. 9(b). The repeatability, hysteresis and vibrations will be controlled with mature closed loop strategies.

- Temperature: Temperature modifies refractive indices and hence the physical propagation loss. The switch is intended to be used at an indoor data centre with temperature control. Current simulations are all carried out at 22°. We repeated the simulation at 25° for P_{31} at 1550 nm, showing that the change is 0.0069 dB in propagation loss and <0.01 dB in coupling loss, whereas the absorption loss remains the same. Coating reflectance requires the details of each surface and this will be carried out in future experiments.

5. Conclusion

In this work, we design and simulate an ultra-fast, low-loss FSO switch, built with a piezo-actuator that laterally shifts the input optical fibre and an optical beam-steering system that completes the switching behaviour. An ultra-fast actuator switching speed of 1.55 μs is estimated for a single connection with a demo circuit. We also propose a physical design process to build a 5×5 non-blocking connectivity. Further, we perform end-to-end simulations for each possible switching path in an optical design software CODE V, showing that a theoretical insertion loss of 2.16 dB is expected for a single connection at optimum alignment, including beam clipping, output fibre coupling, material absorption and coating reflection. In addition, we perform loss sensitivity analysis against beam variations and fibre coupling.

The design is robust against crosstalk between adjacent ports since any beam leakage from fisheye optics to collimator could be blocked by physical barriers. However, the design may suffer from internal crosstalk due to diffraction at the edge clipping of lenses. In terms of manufacturability, the smallest radius of curvature (0.94 mm, S_{21}) and clear aperture radius (0.5 mm, S_1) are both within current industrial capabilities.

Compared with existent FSO based switches such as POLATIS, MEMS and DMD switches, we demonstrate a design prototype that could potentially reach a balance between microseconds switching speed and low insertion loss, by exploiting the benefits from piezo-actuator for fast switching with minimised displacement, and lens optics for displacement compensation and loss control. In our work, the theoretical switching speed shows order of improvements by reducing the actuator load to a lightweight fibre and minimising the mechanical actuation <5 μm than POLATIS and MEMS switches. This work also shows a better loss performance than DMDs by eliminating diffractive optics. The experimental validation will be carried out in future works.

Appendix A: Demo amplifier circuit setup for driving the piezo-actuator

The experimental setups for driving the piezo-actuator PN5FC3-18UM is shown in Fig. 13(a). The piezo-actuators could generate a maximum free load stroke of ±9 μm in either X/Y-axis within the full voltage range of ±200 V. This setup has a limited input voltage of maximum 10 V peak-to-peak from a signal generator. The voltage response is measured on an oscilloscope with a calibrated 10× probe.

The displacement of a piezo-actuator has a nonlinear relationship against driving voltage, shown as hysteresis in Fig. 13(b), requiring ±125 V to reach 50% of the maximum stroke. Therefore, this amplifier setup could theoretically provide $\pm((248.43/2)/125) * (9/2) = \pm 4.47$

Optics EXPRESS

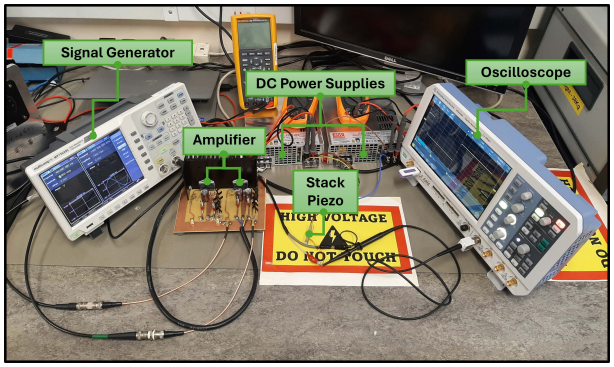

(a)

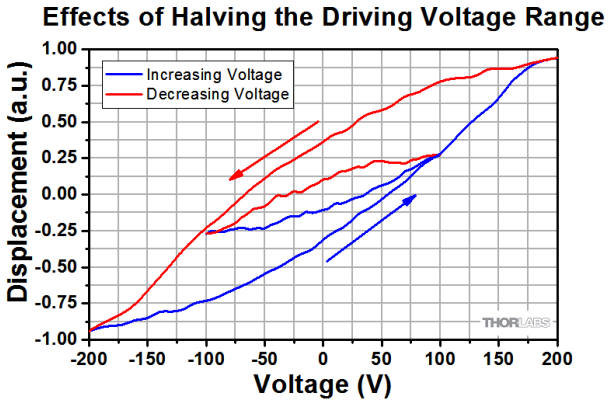

(b)

Fig. 13. (a) Demo amplifier circuit setup for driving the piezo-actuator PN5FC3-18UM. (b)An example response of hysteresis on piezo-actuator displacement by halving the driving voltage from the full range of ±200 V to ±100 V. Source: [32].

μm. The transition time required to switch from 0 to 4.47 μm is (248.43/2)/80.02 = 1.55 μs. Between the two furthermost ports in Fig. 1(b), the piezo-actuator needs to switch from 0 to 4.77 μm. This 0.3 μm error (6%) is within the empirical fluctuation range of 20% of the piezo-actuator and therefore we could approximate the switching latency as 1.55 μs. The precise displacement generated by piezo-actuator will be verified with interferometers in future experiments.

By replacing the input signal generator with a digital-to-analogue converter (DAC), we could maximise the output voltage of the amplifier to achieve the full displacement range of ±200 V. Furthermore, the piezo-actuators will be mounted on customised rigid supports at the base to enhance the reliability and repeatability of controlled movements.

Appendix B: Optical path design in a symmetrical non-blocking switch

We use the switching path P_{32} connecting between Port 3 and Port 2 highlighted in Fig. 14(a) as an example with the following design parameters:

1. Positioning of collimators at the ingress (IN/SMCs):

   As shown in Fig. 14(a), the beam-steering system at the ingress of the switch (IN/BS) has a back focal length F_f<0 measured from the last surface of the fisheye optics that refocuses each steering beam at a virtual focal point A. For the best collimation, A should be

Optics EXPRESS

coincident with the real focal point of any singlet micro-collimator at the ingress (IN/SMC). Therefore, the front surface of each IN/SMC is defined as α-tilt and Y-decentered (Y_{ts}). In CODE V, this shifts the local coordinates starting from this and all subsequent surfaces with respect to a reference coordinate of the main optical axis, where α is the Y-Z plane rotation angle left-handed about +X axis and decenter is the difference between local and reference origins [46]. Numerically, α is equivalent to the slope angle of beam center, whereas Y_{ts}, Z_{ts} are the projections of IN/SMC focal length F_s, respectively. Due to inhomogeneity of fisheye optics, α is approximated with both +/− meridional rays.

$$\tan\alpha = \frac{\mathrm{TANY}^{-} + \mathrm{TANY}^{+}}{2} \tag{4a}$$

$$Y_{ts} = F_s \sin\alpha \tag{4b}$$

$$Z_{ts} = F_s \cos\alpha + F_f \tag{4c}$$

2. FSO propagation distance:

   The beam should be refocused by the collimator at the egress of the switch (OUT/SMC) at another virtual focal point A', located at an image height of H defined in global coordinates relative to the center of IN/BS. This translates to a minimum FSO propagation distance T_{FSO} required to allow for adjacent ports with sufficient mounting pitch $P > R_{\mathrm{CA}}^{\max}$, where $R_{\mathrm{CA}}^{\max}$ is the maximum clear aperture radius. ι is the thickness of a single SMC.

$$(2F_s + T_{\mathrm{FSO}} + 2\iota)\sin\alpha > 2P \tag{5}$$

3. Positioning of collimators (OUT/SMC) and beam-steering system (OUT/BS) at the egress:

   Starting from the front surface of IN/SMC, the effect of decenter and tilt will continue to apply in subsequent local surface coordinates until they are shifted back at OUT/BS. CODE V executes decenters prior to angular tilts and therefore we use dummy surfaces for easy definitions. Assuming the rear surface of an OUT/SMC is indexed as S_r, a dummy surface S_{r+1} is placed after with a thickness of T_{rs} such that the beam continues to propagate in α. Then, a dummy surface S_{r+2} is placed with zero thickness. Then, the first surface of fisheye optics (S_{r+3}) in OUT/BS is defined Y-decentered with Y_{rf} and α'-tilted with respect

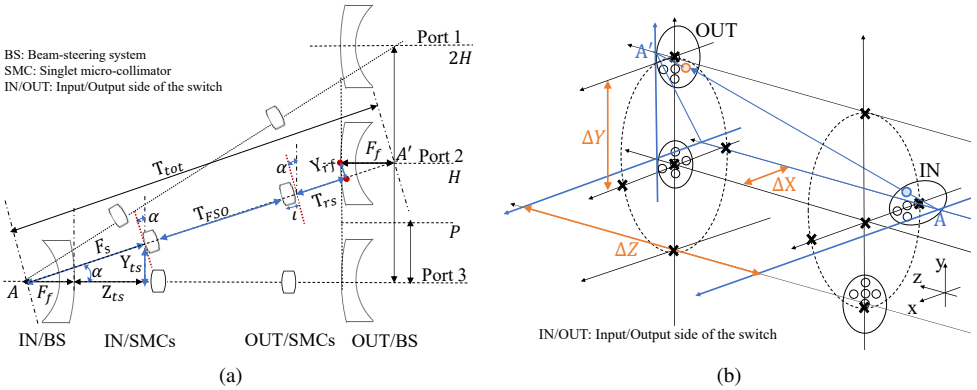

(a) (b)

Fig. 14. (a) Design of optical path P_{32} for Port 3 connecting to Port 2. (b) Side view of cross-axis communication P_{41}. Black lines and circles: global coordinates of fisheye optics. Blue: γ-tilt plane. A and A': virtual focal points of fisheye optics at either input or output side of the switch.

Optics EXPRESS

to S_{r+2}. This removes any angular tilt in the following surfaces but preserves lens center in the global coordinate as H.

$$T_{rs} = F_s + F_f \cos\alpha \tag{6a}$$

$$Y_{rf} = -F_f \sin\alpha \tag{6b}$$

$$\alpha^{'} = -\alpha \tag{6c}$$

The optical path to connect between Port 3 and Port 1 follows the same design process; however, two conditions must be satisfied to maintain symmetricity: (1) the virtual image height of optical path P_{31} should reach exactly $2H$, and (2) the vertex of the first surface of fisheye optics in OUT/BS should be aligned at the same Z coordinate for all ports. This translates to α-tilt and T_{FSO} specifically required as follows, where subscripts i, j represent Port i connecting to j in a single direction, and $T_{32}^{tot} = 2F_s + T_{32}^{FSO} + 2\iota$ is the total optical path between AA'.

$$\tan\alpha_{31} = 2\tan\alpha_{32} \tag{7a}$$

$$T_{31}^{FSO} = \frac{T_{32}^{tot}\cos\alpha_{32}}{\cos\alpha_{31}} - 2F_s - 2\iota \tag{7b}$$

The optical path P_{33} to connect between Port 3 and Port 3 uses the neutral state of piezo-actuator with its parameters given as,

$$\alpha_{33} = \alpha'_{33} = 0 \tag{8a}$$

$$Z_{ts} = T_{rs} = F_f + F_s \tag{8b}$$

$$Y_{ts} = Y_{rf} = 0 \tag{8c}$$

For cross-axis communications between X-Y plane in Fig. 4(b), we use lowercase y, γ to represent piezo-actuator displacement, and uppercase Y, H to represent fabrication data in global coordinates. The optical path P_{41} is highlighted as an example where Port 4 connects to Port 1. The local positioning of SMC is now super-positioned on a γ-tilt plane defined as the rotation in X-Y plane right-handed about the $+Z$ axis [46], i.e. $\gamma_{41} = -45°$ and $y_{41} = \sqrt{2}y_{32}$ in object plane. In global coordinates, as shown in Fig. 14(b), the location of virtual focal points AA' on the optical axis of each port are already deterministic in prior design. Their differences are given as $\Delta X = H_{32}$, $\Delta Y = H_{31} - H_{32} = H_{32}$ and $\Delta Z = -2F_f + Z_{ff}$, where Z_{ff} is the $Z-$difference between vertices of fisheye optics at either ingress or egress of the switch. Therefore, the path design along γ-plane are given as,

$$T_{41}^{tot} = AA' = \sqrt{\Delta X^2 + \Delta Y^2 + \Delta Z^2} \tag{9a}$$

$$T_{41}^{FSO} = T_{41}^{tot} - 2F_s - 2\iota \tag{9b}$$

$$H_{41} = \sqrt{\Delta X^2 + \Delta Y^2} \tag{9c}$$

$$\gamma_{41} = -\arctan\left(\frac{\Delta X}{\Delta Y}\right) \tag{9d}$$

$$\alpha_{41} = \arctan\left(\frac{H_{41}}{\Delta Z}\right) \tag{9e}$$

Due to the presence of aberration, all positioning parameters calculated need fine-tuning in simulation, where H and global Z-coordinates of fisheye vertices are harsh fabrication requirements that must be fulfilled by tuning other parameters. The errors between calculated and simulated values are within 1 decimal place of millimeter.

Optics EXPRESS

Appendix C: Simulation accuracy

The tight input Gaussian beam radius of 0.5 μm into *Beam Synthsis Propagation (BSP)* induces beam radius broadening to 0.75 μm at the initial reconstruction at the Object plane, and same for input radius of 0.8 μm broadening to 0.92 μm. This is because such a tightly focused beam contains evanescent energy that cannot propagate. BSP removes the evanescent components and the remaining field is left with a broadening radius.

At the Image plane (S_{71}), the fast converging beam envelope also gives inaccuracy when integrating the power over the sampling grid. A suitable approximation of the output power is sampled at the last optical surface (S_{70}) before Image Plane to calculate propagation loss in Eq. (3).

Appendix D: Discussions

Figure 15 demonstrates detailed loss contribution at long (1555 nm) and short (1548 nm) wavelengths that previously shown in Fig. 12. This shows that the switch has a stable loss performance in a 7 nm bandwidth. Wavelengths outside this range induce ray tracing failures, and will be tested with a physical switch in future works.

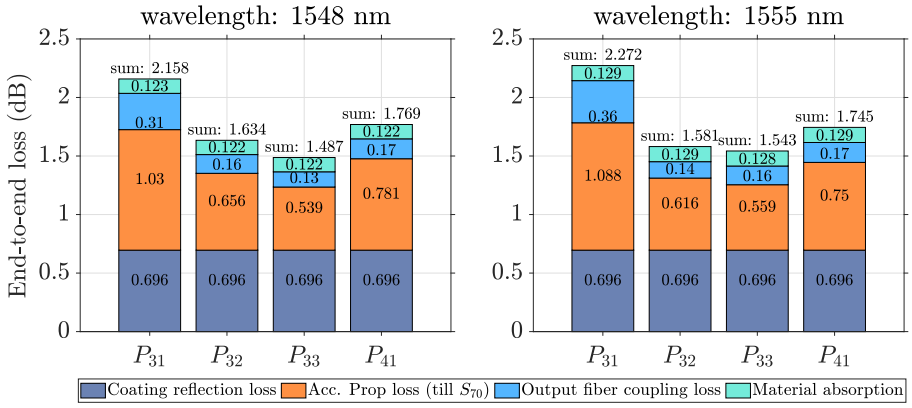

Fig. 15. Loss summary at long (1555 nm) and short (1548 nm) wavelengths for Fig. 12.

Funding. British Telecommunications (Industrial Cooperative Awards in Science and Technology); Engineering and Physical Sciences Research Council (OptoCloud (EP/T026081/1), TRANSNET (EP/R035342/1)).

Disclosures. The authors have no conflicts of interest to declare.

Data availability. Data underlying the results presented in this paper are not publicly available at this time but may be obtained from the authors upon reasonable request.

References

1. Y. Lu and H. Gu, "Flexible and scalable optical interconnects for data centers: Trends and challenges," IEEE Commun. Mag. **57**(10), 27–33 (2019).
2. C. Kachris and I. Tomkos, "A survey on optical interconnects for data centers," IEEE Commun. Surv. Tutorials **14**(4), 1021–1036 (2012).
3. C. Chaintoutis, B. Shariati, A. Bogris, *et al.*, "Free space intra-datacenter interconnects based on 2d optical beam steering enabled by photonic integrated circuits," Photonics **5**(3), 21 (2018).
4. G. Wang, D. G. Andersen, M. Kaminsky, *et al.*, "C-through: Part-time optics in data centers," SIGCOMM Comput. Commun. Rev. **40**(4), 327–338 (2010).
5. G. N. Rouskas and L. Xu, *Optical Packet Switching* (Springer US, Boston, MA, 2005), pp. 111–127.
6. C. W. F. Parsonson, Z. Shabka, W. K. Chlupka, *et al.*, "Optimal control of soas with artificial intelligence for sub-nanosecond optical switching," J. Lightwave Technol. **38**(20), 5563–5573 (2020).
7. S. Chua and B. Li, "1 - introduction to optical switches," in *Optical Switches*, B. Li and S. J. Chua, eds. (Woodhead Publishing, 2010), Woodhead Publishing Series in Electronic and Optical Materials, pp. 1–4.

Optics EXPRESS

8. M. Stepanovsky, "A comparative review of mems-based optical cross-connects for all-optical networks from the past to the present day," IEEE Commun. Surv. Tutorials **21**(3), 2928–2946 (2019).
9. Q. Cheng, S. Rumley, M. Bahadori, *et al.*, "Photonic switching in high performance datacenters }invited\protect \inlinegif {," Opt. Express **26**(12), 16022–16043 (2018).
10. HUBER+SUHNER-POLATIS, "Polatis 576- 576×576 port software-defined optical circuit switch," Available at https://www.polatis.com/polatis576.asp.
11. E. H. Cook, S. J. Spector, M. G. Moebius, *et al.*, "Polysilicon grating switches for lidar," J. Microelectromech. Syst. **29**(5), 1008–1013 (2020).
12. X. Zhang, K. Kwon, J. Henriksson, *et al.*, "A large-scale microelectromechanical-systems-based silicon photonics lidar," Nature **603**(7900), 253–258 (2022).
13. L. Qiao, W. Tang, and T. Chu, "32 ×32 silicon electro-optic switch with built-in monitors and balanced-status unitsc," Sci. Rep. **7**(1), 42306 (2017).
14. T. Chu, N. Chen, W. Tang, *et al.*, "Large-scale high-speed photonic switches fabricated on silicon-based photonic platforms," in *2023 Optical Fiber Communications Conference and Exhibition (OFC)*, (2023), pp. 1–3.
15. D. C. Kilper and R. S. Tucker, "Chapter 17 - energy-efficient telecommunications," in *Optical Fiber Telecommunications (Sixth Edition)*, I. P. Kaminow, T. Li, and A. E. Willner, eds. (Academic Press, Boston, 2013), Optics and Photonics, pp. 747–791, sixth edition ed.
16. A. Jahid, M. H. Alsharif, and T. J. Hall, "A contemporary survey on free space optical communication: Potentials, technical challenges, recent advances and research direction," Journal of Network and Computer Applications **200**, 103311 (2022).
17. A. S. Hamza, J. S. Deogun, and D. R. Alexander, "Free space optical data center architecture design with fully connected racks," in *2014 IEEE Global Communications Conference*, (2014), pp. 2192–2197.
18. A. S. Hamza, J. S. Deogun, and D. R. Alexander, "Wireless communication in data centers: A survey," IEEE Commun. Surv. Tutorials **18**(3), 1572–1595 (2016).
19. I. K. Son and S. Mao, "A survey of free space optical networks," Digital Communications and Networks **3**(2), 67–77 (2017).
20. M. Ghobadi, R. Mahajan, A. Phanishayee, *et al.*, "Projector: Agile reconfigurable data center interconnect," in *Proceedings of the 2016 ACM SIGCOMM Conference*, (Association for Computing Machinery, New York, NY, USA, 2016), SIGCOMM '16, p. 216–229.
21. N. Hamedazimi, Z. Qazi, H. Gupta, *et al.*, "Firefly: A reconfigurable wireless data center fabric using free-space optics," in *Proceedings of the 2014 ACM Conference on SIGCOMM*, (Association for Computing Machinery, New York, NY, USA, 2014), SIGCOMM '14, pp. 319–330.
22. S. Zhang, R. Kraemer, B. Pan, *et al.*, "Experimental assessment of a novel optical wireless data center network architecture," in *2020 European Conference on Optical Communications (ECOC)*, (2020), pp. 1–4.
23. J. Li, Q. Zhang, and A. Liu, "Advanced fiber optical switches using deep rie (drie) fabrication," Sens. Actuators, A **102**(3), 286–295 (2003).
24. C. Jia, J. Zhou, W. Dong, *et al.*, "Design and fabrication of silicon-based 8×8 mems optical switch array," Microelectron. J. **40**(1), 83–86 (2009).
25. K.-C. Fan, W.-L. Lin, L.-H. Chiang, *et al.*, "A 2× 2 mechanical optical switch with a thin mems mirror," J. Lightwave Technol. **27**(9), 1155–1161 (2009).
26. Y. Han, Z. Li, L. Wu, *et al.*, "High-speed two-dimensional spectral-scanning coherent lidar system based on tunable vcsel," J. Lightwave Technol. **41**(2), 412–419 (2023).
27. L. Wu, Y. Han, Z. Li, *et al.*, "12 gbit/s indoor optical wireless communication system with ultrafast beam-steering using tunable vcsel," Opt. Express **30**(9), 15049–15059 (2022).
28. H. Choi, N.-C. Park, and W.-C. Kim, "Optical system design for light detection and ranging with ultra-wide field-of-view using liquid lenses," Microsyst. Technol. **26**(1), 121–131 (2020).
29. D. Sabarianand, P. Karthikeyan, and T. Muthuramalingam, "A review on control strategies for compensation of hysteresis and creep on piezoelectric actuators based micro systems," Mechanical Systems and Signal Processing **140**, 106634 (2020).
30. Z. Chi and Q. Xu, "Recent advances in the control of piezoelectric actuators," International Journal of Advanced Robotic Systems **11**(11), 182 (2014).
31. J. Minase, T.-F. Lu, B. Cazzolato, *et al.*, "A review, supported by experimental results, of voltage, charge and capacitor insertion method for driving piezoelectric actuators," Precis. Eng. **34**(4), 692–700 (2010).
32. Thorlabs, "Three bonded discrete piezo stacks, two shear and one longitudinal, 7.0 μm 3d displacement, 5.0 × 5.0 × 18.0 mm, flat end plates," Available at https://www.thorlabs.com/thorproduct.cfm?partnumber=PN5FC3.
33. LaseOptics, "Laseoptics corporation," Available at https://laseoptics.com/.
34. T. Matsuyama, Y. Ohmura, and D. Williamson, "The lithographic lens: Its history and evolution," Proceedings of SPIE - The International Society for Optical Engineering **6154**, 24–37 (2006).
35. R. I. Mercado and T. Matsuyama, "Microlithographic lenses," in *International Optical Design Conference 1998*, vol. 3482 L. R. Gardner and K. P. Thompson, eds., International Society for Optics and Photonics (SPIE, 1998), pp. 664–672.
36. A. Mikš and J. Novák, "Method of initial design of a two-element double-sided telecentric optical system," Opt. Express **31**(2), 1604–1614 (2023).

Optics EXPRESS

37. L. Fan and L. Lu, "Design of a simple fisheye lens," Appl. Opt. **58**(19), 5311–5319 (2019).
38. C. Brauer-Burchardt and K. Voss, "A new algorithm to correct fish-eye- and strong wide-angle-lens-distortion from single images," in *Proceedings 2001 International Conference on Image Processing (Cat. No.01CH37205)*, vol. 1 (2001), pp. 225–228, vol. 1.
39. Thorlabs, "La4026-c - f = 6 mm, Ø2 mm uvfs plano-convex lens, arc: 1050 - 1700 nm," Available at https://www.thorlabs.com/thorproduct.cfm?partnumber=LA4026-C.
40. CodeV, Chapter 3, Beam synthesis propagation (bsp), Code V Generalized Beam Propagation and Coupling Efficiency Reference Manual (Synopsys, Inc., 2022).
41. K. Uehara and H. Kikuchi, "Transmission of a gaussian beam through a circular aperture," Appl. Opt. **25**(24), 4514–4516 (1986).
42. D. M. Marom, "3.07 - optical communications," in *Comprehensive Microsystems*, Y. B. Gianchandani, O. Tabata, and H. Zappe, eds. (Elsevier, Oxford, 2008), pp. 219–265.
43. CodeV, Fibre couping efficiency (cef), Chapter 5, Code V Generalized Beam Propagation and Coupling Efficiency Reference Manual (Synopsys, Inc., 2022).
44. Thorlabs, "Pia25 - piezo inertia actuator, 25 mm travel, Ø3/8" mounting barrel," Available at https://www.thorlabs.com/thorproduct.cfm?partnumber=PIA25.
45. Thorlabs, "Optical coatings," Available at https://www.thorlabs.com/newgrouppage9.cfm?objectgroup_id=5840.
46. CodeV, Defining tilts and decenters, Chapter 9, Code V Lens System Setup Reference Manual (Synopsys, Inc., 2022).